An Energy Management Method Considering the Wide-Range Power Line Current Variation and Output Power Improvement for Free-Standing Magnetic Field Energy Harvester

Huanyu Yang, Yuhang Liu, Yong Li, *Senior Member, IEEE*, Yonghong Zhou, and Zhengyou He, *Senior Member, IEEE*

***Abstract*—Free-standing magnetic field energy harvesters (FSMFEH) have proven potential for powering sensors on power transmission lines. To realize the application FSMFEH, a key challenge is to satisfy the power supply requirements of sensors, i.e., the output power and the constant output voltage requirements. However, the output power and voltage of FSMFEH systems are highly dependent on the power line current, which typically varies over a wide-range. Therefore, the stabilized power supply to the sensor will be broken, and the optimal output power will not be maintained. To address these issues, an energy management circuit with dual-coil FSMFEH and bidirectional dc–dc is proposed in this article. First, the influence of power line currents and the constant voltage output to the system are analyzed. Then, the optimal operating modes of the system under different load conditions are clarified. Finally, the energy management strategies are presented based on the mode switching boundaries of the dual-coil system and the voltage control of the bidirectional dc–dc. Experimental results show that when the power line current varies from 30 to 500 A, the output power can be improved from 0.6 mW to 3.2 mW at the minimum power line current, and from 195 to 365 mW at the maximum power line current.**

***Index Terms*—Dual-coil system, energy management, free-standing magnetic field energy harvesters (FSMFEH), power improving.**

Received 19 August 2025; revised 29 November 2025; accepted 30 December 2025. Date of publication 12 January 2026; date of current version 20 March 2026. This work was supported in part by the Sichuan Science and Technology Program under Grant 2024NSFJQ0011 and in part by the Science and Technology Innovation Program of Hunan Province under Grant 2025JJ60271. Recommended for publication by Associate Editor S. Jeong.*(Corresponding author: Yong Li.)*

Huanyu Yang is with the Key Laboratory of Magnetic Suspension Technology and Maglev Vehicle, Ministry of Education, School of Electrical Engineering, Southwest Jiaotong University, Chengdu 610031, China, and also with Hunan Disaster Prevention Technology Company, Ltd., Changsha 410018, China (e-mail: yanghy@my.swjtu.edu.cn).

Yuhang Liu, Yong Li, Yonghong Zhou, and Zhengyou He are with the Key Laboratory of Magnetic Suspension Technology and Maglev Vehicle, Ministry of Education, School of Electrical Engineering, Southwest Jiaotong University, Chengdu 610031, China (e-mail: yuhang_liu@my.swjtu.edu.cn; yong_li@swjtu.edu.cn; yonghong_zhou@my.swjtu.edu.cn; hezy@swjtu.edu.cn).

Color versions of one or more figures in this article are available at https://doi.org/10.1109/TPEL.2026.3651612.

Digital Object Identifier 10.1109/TPEL.2026.3651612

I. Introduction

POWER lines and busbars are the main carriers to realize the transmission of electric energy in urban distribution networks. To ensure the safety and reliability of the power transmission process, it is necessary to install sensors to realize the collection of temperature, voltage, current, and other information [1], [2]. Generally, these sensors are mainly powered by batteries. However, batteries are required to be replaced due to their limited capacity. As a result, it will cause inconvenience to operators and increase maintenance costs [3].

Recently, environment energy harvesting technology has been rapidly developed, and substantial research has shown the potential in supplying power to sensors through solar [4], [5], wind [6], [7], vibration [8], [9], and magnetic field [10], [11]. Among them, the free-standing magnetic field energy harvesters (FSMFEH) can capture energy from the magnetic field, which is independent of weather, and have higher output power compared with vibration energy harvesters. Therefore, it is attractive to use FSMFEH for a continuous, maintenance-free power supply to sensors in power lines and busbars, the configuration case is shown in Fig. 1.

Power line sensors like HCSP-1BS, CSHV, etc., can consume tens of milliwatts of power on average [12]. To satisfy the power requirement of sensors, it is critical to improve the output power of the FSMFEH systems [13]. Currently, there are two main categories of approaches to improve the output power of FSMFEH systems. On the one hand, as shown in Fig. 1, by optimizing the parameters of harvesters, the output power can be significantly improved. For example, Moghe et al. [14] proposes the I-shape core structure to improve the ability to converge magnetic flux. By optimizing the size of the I-shaped core, the harvested energy is increased. Besides, Yuan et al. [15], [16] proves that increasing the number of coil turns appropriately can also improve the output power. On the other hand, impedance matching is also an effective way to improve the output power by controlling the back-end circuit. In [17], the single-stage ac–dc boost rectifier is adopted, and the optimum power control method is proposed to realize the maximum power point tracking (MPPT) of the energy harvesting system. Similarly, a reconfigurable rectifier and its impedance matching methods are presented in [18]. The output

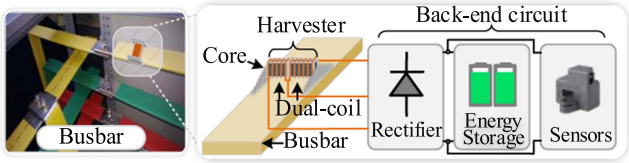

Fig. 1. Configuration case of the FSMFEH system.

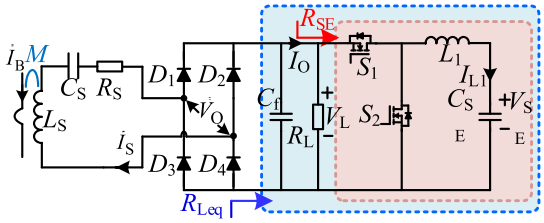

Fig. 2. General FSMFEH system with the bidirectional DC-DC.

power can be maintained above 8.19 mW with a wide load range. However, the maximum output power and the output voltage can be varied due to the varied power line currents. As a result, the output power and voltage of FSMFEH systems will exceed or lower than the rated value when the current of the power line is high or low. Thus, the output of the FSMFEH system struggles to meet practical requirements of the sensor.

To address these issues, a general method is to adopt the energy management circuit to regulate the output voltage or power of the system. In [19], the full-bridge active rectifier is utilized to control the parallelled batteries to realize the energy management. However, the real-time duty cycle control will lead to a high computation burden and switching loss. Moreover, Wang et al. [20] present a three-port interface energy management circuit in which an energy storage battery is connected in parallel with the load as an external port, and the power flow is controlled by a bidirectional dc–dc converter. The experimental results show that the vibration electromagnetic energy harvester can obtain a constant load voltage of 3.3 V and realize the MPPT at a fixed vibration frequency. However, similar to the influence of the varied power line current, the influence of the varied vibration frequency on the energy harvester has not been addressed. In summary, the above researches indicate that there is a lack of an energy management method for FSMFEH systems that takes into account power line current variations and system impedance characteristics to achieve MPPT and constant voltage control.

Thus, in this article, an energy management method is proposed to realize power improvement and constant output voltage control. The main contributions are listed as follows.

1) The effect of power line current variation and the constant output voltage control on the impedance characteristics of a general FSMFEH system with the bidirectional dc–dc is considered and analyzed.
2) Considering the influence of power line current variation on system impedance, a dual-coil and three-bridge FSMFEH system with a bidirectional dc–dc is proposed. Operation principles and load characteristics are clarified and modeled.
3) The energy management strategies for the system are presented with the consideration of wide-range power line current variation. The proposed strategies provide guidance for constant voltage control of bidirectional dc–dc and mode switching boundaries of a dual-coil system, which realizes the output power improvement and constant voltage output control.

The rest of this article is structured as follows. In Section II, the influence of the power line current variation on FSMFEH systems is introduced. Considering the wide range variation of the equivalent load, the dual-coil and three-bridge rectifier systems are proposed, and mathematical models under different operation models are derived. In Section III, based on the model switching boundary and the voltage control of the bidirectional dc–dc, the energy management strategies are designed to deal with the wide range variation of the power line current. Then, four typical power line current cases with corresponding control logic have been clarified. In Section IV, the constant voltage control, the output power improvement, as well as the accuracy of model switching, are verified through experiments. Finally, Section V concludes this article.

TABLE I
SYSTEM PARAMETERS

Sym.	*value*	*Sym.*	*value*
I_B	100/60 A	M	286 μH
L_1	1000 μH	R_S	568 Ω
C_{SE}	1 F	V_{ref}	3.3 V

II. Operation Principles of the Proposed System

A. Influence of Power Line Current on FSMFEH Systems

As shown in Fig. 2, L_S is the self-induction of the energy harvesting coil, C_S is the series resonant capacitor. C_f is the filter capacitor, and C_{SE} is the energy storage supercapacitor (SC). V_O is the ac port voltage of the rectifier. V_L is the dc voltage across the load R_L. V_{SE} is the dc voltage across the energy storage capacitor C_{SE}. I_{L1} is the average current flowing through the inductor. The full-bridge rectifier consists of diodes D_1–D_4. The bidirectional buck-boost converter is composed of MOSFETs S_1–S_2 and inductor L_1. For a single-coil and full-bridge rectifier FSMFEH system with the bidirectional dc–dc and energy storage, the equivalent dc load R_{Leq} can be considered as the parallel connection of load R_L and the equivalent energy storage load R_{SE}

$$R_{Leq} = R_L // R_{SE} = \frac{V_L}{I_O}. \tag{1}$$

When the output voltage V_L is controlled at a constant voltage by the dc–dc, the output current I_O will change as the power line current $\dot{I}_B$ changes. Thus, the equivalent load R_{Leq} of the system will change accordingly with the fluctuation of the power line current. Based on the parameters in Table I, the simulation results can be developed, and the impact of power line current on the equivalent load R_{Leq} can be analyzed.

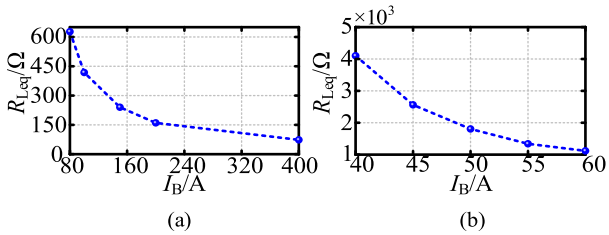

Fig. 3. Variation curve of R_{Leq}. (a) When the power line current is high. (b) When the power line current is low.

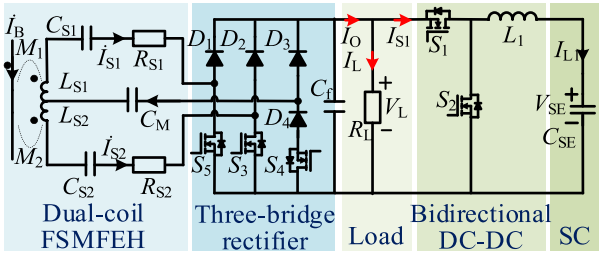

Fig. 4. Proposed energy management circuit.

As shown in Fig. 3(a), when power line current is high, i.e., I_B increases from 80 to 400 A, R_{Leq} decreases from 600 to 73 Ω. Even worse, as shown in Fig. 3(b), when the power line current varies from 40 to 60 A, R_{Leq} dramatically varies from 4000 to 1000 Ω. Both cases present that when the power line current changes, the equivalent load will vary widely under constant output voltage control. As a result, the output power will inevitably decrease compared with the optimal output power point. Therefore, it is important for FSMFEH system to realize both impedance matching and output voltage control.

B. Operation Principles of Dual-coil and Three-Bridge Rectifier Systems

The proposed energy management circuit for the FSMFEH is shown in Fig. 4, including a dual-coil FSMFEH system, a three-bridge rectifier, a bidirectional dc–dc, and an SC. The dual-coil and the three-bridge rectifier develop the impedance matching circuits to improve the output power under different power line current conditions. Meanwhile, by controlling the bidirectional dc–dc and the SC, the constant output voltage of the FSMFEH system can be regulated. The parameters are introduced as follows. $\dot{I}_{S1}$ and $\dot{I}_{S2}$ represent the current of the harvesting coil L_{S1} and L_{S2}. R_{S1} and R_{S2} denote the parasitic resistance of L_{S1} and L_{S2}. C_{S1}, C_{S2}, and C_M are resonant capacitors. Moreover, M_1 and M_2 are the mutual inductances between the cable and harvester coils. R_L is the sensor load. In addition, the dc–dc includes an inductor L_1 and two switches (S_1, S_2). The rectifier consists of four diodes (D_1-D_4) and three switches (S_3, S_4, S_5).

To simplify the analysis, the output load of the FSMFEH system is considered as R_{Leq}. Switch S_5 is designed to realize voltage regulation under extreme conditions. Here, S_5 is turned OFF and considered as a diode. Thus, the equivalent circuit of

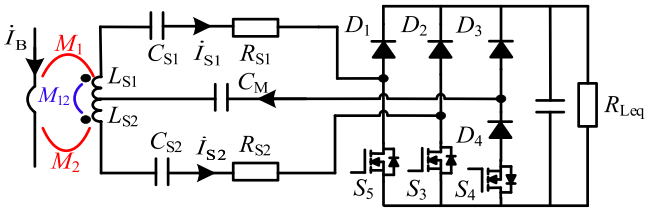

Fig. 5. Equivalent circuit of the proposed FSMFEH system.

TABLE II
OPERATION MODE OF THE SYSTEM

Mode	State
Mode 1 Single channel with a full bridge rectifier (S_3 OFF S_4 OFF)	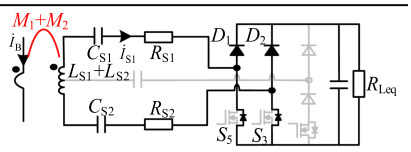
Mode 2 Single channel with a half-bridge rectifier (S_3 ON S_4 OFF)	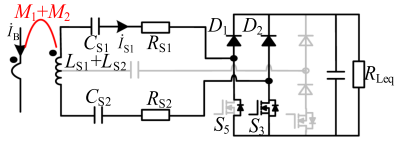
Mode 3 Dual channel with two full-bridge rectifiers (S_3 OFF S_4 ON)	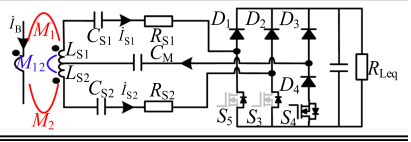

the proposed system in Fig. 4 can be re-depicted as shown in Fig. 5. To make the circuit well-tuned, the relationship should be satisfied

$$\begin{cases} C_{S1} = 1/\omega^2 (L_{S1} - M_{12}) \\ C_{S2} = 1/\omega^2 (L_{S2} - M_{12}) \\ C_M = 1/\omega^2 M_{12} \end{cases} \tag{2}$$

where M_{12} denotes the cross-coupling of L_{S1} and L_{S2}.

Different from the traditional single-stage ac–dc boost rectifier that uses two MOSFETs to achieve the MPPT, the proposed three-bridge rectifier adopts two MOSFETs to change the operation mode of the system instead of dynamically tracking the maximum power point so that additional switching losses can be avoided. Based on these switches, the operation mode of the system can be divided, as given in Table II. It should be clarified that the source of S_4 is connected to the anode of diode D_4. In this configuration, the body diode of S_4 is connected in reverse series with D_4. As a result, the third rectifier leg (S_4+D_4) can be effectively disabled when S_4 is OFF.

Since the third bridge arm is disabled in mode 1 and mode 2, the equivalent ac circuit of the energy harvesting system remains consistent. The difference is that the variation of the rectifier bridge topology in mode 1 and mode 2 leads to changes in the equivalent ac load. To distinguish the simplified circuits of mode 1 and mode 2, R_O is adopted to denote the equivalent load of the full-bridge rectifier, while R_{OH} denotes the equivalent load of the half-bridge rectifier, as shown in Fig. 6(a) and (b).

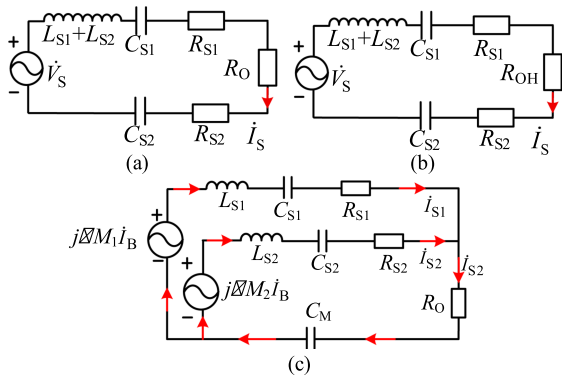

Fig. 6. Simplified circuit. (a) Mode 1. (b) Mode 2. (c) Mode 3.

Mode 1: The simplified circuit of mode 1 is shown in Fig. 6(a). R_O is the equivalent ac load. According to Faraday's law, the induced voltage $\dot{V}_S$ can be represented as

$$\dot{V}_S = j\omega\left(M_1 + M_2\right)\dot{I}_B. \tag{3}$$

By using the fundamental component approximation method, the KVL equations of the circuit can be obtained as

$$V_S = I_S\left(R_{S1} + R_{S2} + R_O\right) \tag{4}$$

where I_B, I_S, and V_S are the root-mean-square (RMS) values of $\dot{I}_B$, $\dot{I}_S$, and $\dot{V}_S$.

The relationship between the equivalent ac load R_O and the equivalent dc load R_{Leq} is

$$R_O = \frac{8}{\pi^2}R_{Leq}. \tag{5}$$

According to (3) and (4), the output power can be calculated as

$$\begin{aligned} P_O &= \frac{{V_S}^2}{\left(R_{S1} + R_{S2} + R_O\right)^2}R_O \\ &= \frac{\omega^2\left(M_1 + M_2\right)^2{I_B}^2}{\left(R_{S1} + R_{S2} + \frac{8}{\pi^2}R_{Leq}\right)^2}\left(\frac{8}{\pi^2}R_{Leq}\right). \end{aligned} \tag{6}$$

Setting the derivative of P_O to 0, the optimal load can be obtained as

$$R_{\mathrm{LSFopt}} = \frac{\pi^2}{8}\left(R_{S1} + R_{S2}\right). \tag{7}$$

The maximum output power can be calculated by setting $R_{Leq} = R_{\mathrm{LSFopt}}$

$$P_{O\mathrm{opt}-1} = \frac{\left(\omega I_B\left(M_1 + M_2\right)\right)^2}{4\left(R_{S1} + R_{S2}\right)}. \tag{8}$$

Mode 2: The simplified circuit of mode 2 is shown in Fig. 6(b). The relationship between R_{OH} and R_{Leq} with the half-bridge rectifier becomes [21]

$$R_{\mathrm{OH}} = \frac{2}{\pi^2}R_{Leq}. \tag{9}$$

Based on the KVL law, the following equation for the circuit in mode 2 can be obtained as

$$\dot{I}_S R_{\mathrm{OH}} = j\omega\left(M_1 + M_2\right)\dot{I}_B - \dot{I}_S\left(R_{S1} + R_{S2}\right). \tag{10}$$

The output power in this mode can be calculated as

$$\begin{aligned} P_O &= I_S^2 R_{\mathrm{OH}} \\ &= \frac{\omega^2\left(M_1 + M_2\right)^2{I_B}^2}{\left(R_{S1} + R_{S2} + \frac{2}{\pi^2}R_{Leq}\right)^2}\left(\frac{2}{\pi^2}R_{Leq}\right). \end{aligned} \tag{11}$$

Similarly, by setting the derivative of P_O to 0, the optimal load in mode 2 can be calculated as

$$R_{\mathrm{LSHopt}} = \frac{\pi^2}{2}\left(R_{S1} + R_{S2}\right). \tag{12}$$

The maximum output power in mode 2 can be calculated by setting $R_{Leq} = R_{\mathrm{LSHopt}}$

$$P_{O\mathrm{opt}-2} = \frac{\left(\omega I_B\left(M_1 + M_2\right)\right)^2}{4\left(R_{S1} + R_{S2}\right)}. \tag{13}$$

According to (8) and (13), it can be seen that the maximum output power $P_{O\text{opt-2}}$ of mode 2 is the same as that of mode 1.

Mode 3: The simplified circuit of mode 3 is shown in Fig. 6(c). When S_3 is OFF and S_4 is ON, the dual coils are connected with the full bridge rectifier. According to the KVL law, the following equation should be satisfied as

$$\begin{cases} \left(\dot{I}_{S1} + \dot{I}_{S2}\right)R_O = j\omega M_1\dot{I}_B - \dot{I}_{S1}R_{S1} \\ \left(\dot{I}_{S1} + \dot{I}_{S2}\right)R_O = j\omega M_2\dot{I}_B - \dot{I}_{S2}R_{S2} \end{cases}. \tag{14}$$

The output power in mode 3 can be calculated as

$$\begin{aligned} P_O &= \left(I_{S1} + I_{S2}\right)^2 R_O \\ &= \frac{\omega^2\left(M_1 + M_2\right)^2{I_B}^2}{\left(R_{S1} + R_{S2} + \frac{32}{\pi^2}R_{Leq}\right)^2}\left(\frac{32}{\pi^2}R_{Leq}\right). \end{aligned} \tag{15}$$

Similarly, the optimal load in mode 3 can be calculated as

$$R_{\mathrm{LDFopt}} = \frac{\pi^2}{32}\left(R_{S1} + R_{S2}\right). \tag{16}$$

The maximum output power in mode 3 can be calculated by setting $R_{Leq} = R_{\mathrm{LDFopt}}$

$$P_{O\mathrm{opt}-3} = \frac{\omega^2\left(M_1 + M_2\right)^2{I_B}^2}{4\left(R_{S1} + R_{S2}\right)}. \tag{17}$$

It can be observed that the maximum output power in three modes is theoretically the same according to (8), (13), and (17). More importantly, according to (7), (12), and (16), the optimal load condition satisfies: $R_{\mathrm{LDFopt}} < R_{\mathrm{LSFopt}} < R_{\mathrm{LSHopt}}$. As a result, the diagram of output power varying with equivalent load under different modes is shown in Fig. 7. Compared with the single operation mode, the output power can be improved by switching the operation mode of the rectifier under different load conditions.

III. Energy Management Strategies

To improve the output power and achieve the constant voltage output for the load under the wide-range variation of the power line current, the energy management strategies are presented as follows.

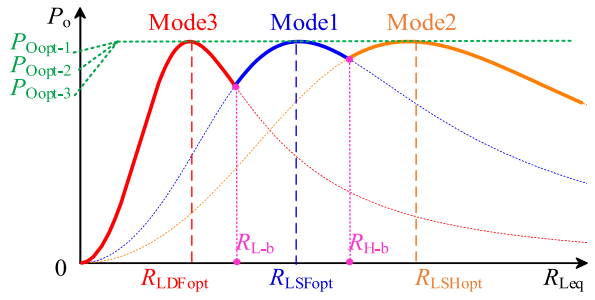

Fig. 7. Diagram of output power varying with load under different modes.

Besides, according to Fig. 7, the output power in mode 3 is higher than in mode 1 and mode 2 when the equivalent dc load R_{Leq} is lower than the boundary $R_{L\text{-}b}$. Therefore, the load switching boundary of mode 3 to mode 1 can be calculated as

$$R_{L-b} = \frac{\pi^2}{16}\left(R_{S1} + R_{S2}\right). \tag{18}$$

Similarly, the output power in mode 2 is higher than in mode 1 and mode 3 when R_{Leq} is higher than the boundary $R_{H\text{-}b}$. Then, $R_{H\text{-}b}$ can be calculated as

$$R_{H-b} = \frac{\pi^2}{4}\left(R_{S1} + R_{S2}\right). \tag{19}$$

It is worth noting that S_3 will turn ON in mode 2, while S_4 will turn ON in mode 3. Therefore, by comparing the load value of the FSMFEH system and turning ON the corresponding switch, the mode switching and output impedance regulation can be achieved.

Considering the wide-range power line current variations, four different operation cases are analyzed here. The diagram of the energy flow under different power line current conditions is depicted in Fig. 8.

Case 1: Power line current is high so that the output power (P_o) of the FSMFEH system is higher than the load required (P_L), i.e., $P_o > P_L$. In this case, the bidirectional dc–dc needs to operate in buck mode to charge the SC and maintain a stable load voltage V_L, the power flow is shown in Fig. 8(a). According to (1), the equivalent dc load R_{Leq} can be obtained by sampling V_L and I_o. Also, the optimal operation mode can be determined by comparing the value of R_{Leq}, $R_{H\text{-}b}$, and $R_{L\text{-}b}$.

Case 2: Power line current is low, which means the output power P_o of the FSMFEH system cannot sufficiently power the load, i.e., $P_o < P_L$. The bidirectional dc–dc needs to operate in boost mode to let the SC discharge to the load. At this time, the power flow is shown in Fig. 8(b). According to (1), I_o will decrease and R_{Leq} will increase in this case. Thus, the operation mode should be redetermined.

Case 3: Power line current is just enough to power load, i.e., $P_o = P_L$. The bidirectional dc–dc needs to stop charging/discharging the SC, the power flow is shown in Fig. 8(c). In fact, this case is a transition between *case* 1 and *case* 2, and it lasts for a short period of time when power line current varies.

Case 4: Power line current continues to decrease, the output power of the FSMFEH system cannot power the load, which is a special case of *case* 2. The load needs to be powered by the SC. The bidirectional dc–dc should operate in Boost mode. The power flow is shown in Fig. 8(d).

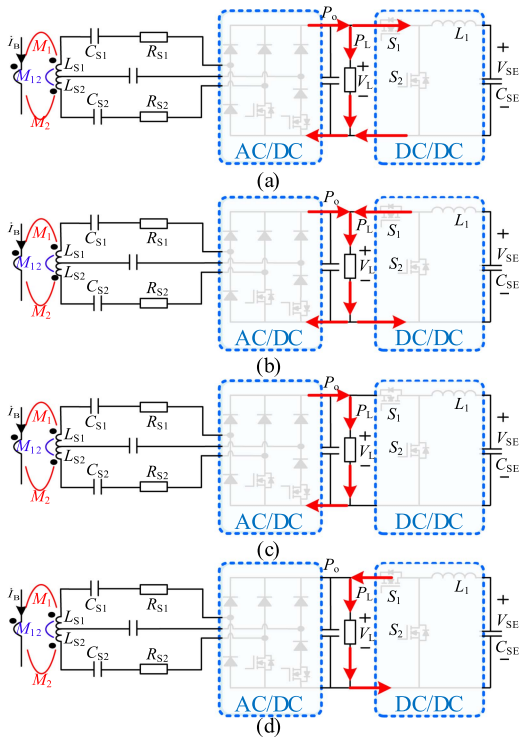

Fig. 8. Power flow under different power line current conditions. (a) Case 1. (b) Case 2. (c) Case 3. (d) Case 4.

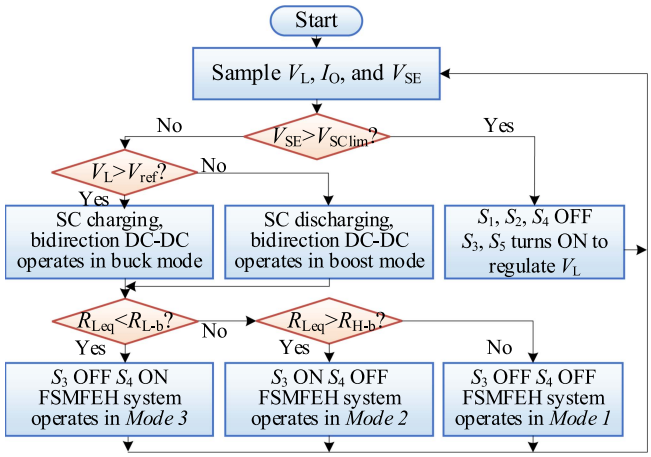

Fig. 9. Energy management strategies of the proposed system.

According to the analysis above, the energy management strategies are proposed to enable the FEMFEH system to adapt to the variation of the power line current. The proposed energy management strategies are shown in Fig. 9, and the control diagram of the proposed dual-coil FEMFEH system is shown in Fig. 10. When the SC is not fully charged, i.e., $V_{SE} < V_{SClim}$, the output voltage V_L should be compared with reference output voltage V_{ref} to determine the buck/boost mode of dc–dc.

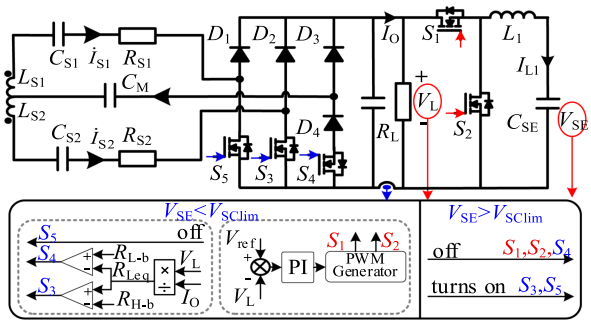

Fig. 10. Control diagram of the proposed dual-coil FEMFEH system with a bidirectional DC–DC.

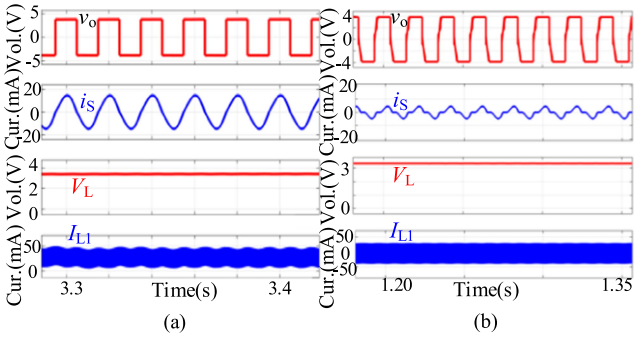

Fig. 11. Simulation waveforms. (a) Mode 1, $I_B = 100$ A. (b) Mode 1, $I_B = 60$ A.

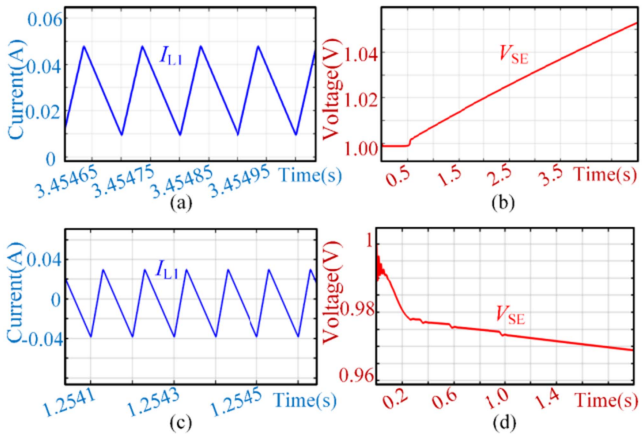

Fig. 12. Microscopic waveform. (a) Charging current waveform ($I_B = 100$ A). (b) Charging voltage waveform ($I_B = 100$ A). (c) Discharging current waveform ($I_B = 60$ A). (d) Discharging voltage waveform ($I_B = 60$ A).

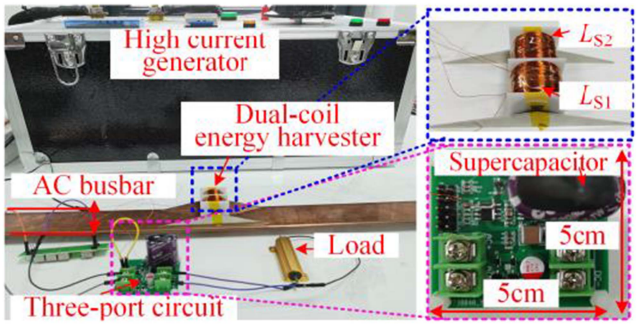

Fig. 13. Experimental platform of the proposed system.

Then, comparators are required to enable the mode switching of the dual-coil and three-bridge rectifier. When $R_{\mathrm{Leq}} > R_{\mathrm{H\text{-}b}}$, S_3 should turn ON, and the system will operate in mode 2. When $R_{Leq} < R_{L\text{-}b}$, S_4 should turn on, and the system will operate in mode 3. Otherwise, S_3, S_4 should turn OFF, and the system will operate in mode 1. Besides, when the SC is fully charged, S_1, S_2, and S_4 should turn OFF to stop the SC charging. Under these extreme conditions, S_3 and S_5 should turn ON; by regulating the duty cycle of S_3 and S_5, V_L can be controlled [22].

Fig. 11 shows the simulation waveforms in typical operation conditions. v_o and i_s denote the input ac voltage and current of the rectifier. When the power line current is high, e.g., $I_B = 100$ A, the simulation results are shown in Fig. 11(a). The load voltage V_{L} can be stably maintained at 3.3V. Meanwhile, I_{L1} is positive, indicating FSMFEH system is charging the SC at this time. Fig. 12(a) shows the microscopic waveform of I_{L1} during the charging process. Obviously, bidirectional dc–dc is in the continuous conduction mode (CCM). The initial value of the voltage V_{SE} of the SC is 1 V, and its charging waveform is shown in Fig. 12(b), which gradually increases. When the power line current is low, e.g., $I_B = 60$ A, the simulation results are shown in Fig. 11(b). The load voltage V_{L} can also be stably maintained at 3.3 V. Similarly, Fig. 12(c) shows the microscopic waveform of I_{L1} during the switching cycle, and the bidirectional dc–dc is also in the CCM. In addition, I_{L1} is negative, indicating that the SC is discharging and supplying power to the load at this time. The initial value of the voltage V_{SE} of the SC is 1 V, and its discharge waveform is shown in Fig. 12(d), and the V_{SE} gradually decreases.

There are two advantages of this strategy. On the one hand, unlike the traditional method that requires duty cycle control to realize the MPPT, in this method, MOSFETs of the three-bridge rectifier only switch once within the specified load range. Thus, the switching loss of the three-bridge rectifier can be limited, and the control can be easily implemented.

On the other hand, according to the energy management strategies, the energy storage system only discharges when the power line current is low. Therefore, the energy of the SC/batteries can be preserved as much as possible to provide power to the load when the power line current is low, or there is a line fault. As a result, the reliable power supply of the sensors under extreme operating conditions can be ensured.

IV. Experimental Validation

A. Experimental Prototype

As shown in Fig. 13, a prototype is built to investigate the performance of the proposed system. A high current generator is used to form a 50 Hz ac current to simulate the busbar. Specific parameters are given in Table III. The details of the core shape and material are provided in Fig. 14. The core is composed of a

TABLE III
SYSTEM PARAMETERS

Sym.	*Value*	*Sym.*	*Value*	*Sym.*	*Value*
M_1, M_2	143 μH	C_{s1}	7.09 μF	S_1-S_4	PMV30UN2R
R_{S1}, R_{S2}	284 Ω	C_{s2}	7.366 μF	D_1-D_5	CUS10S30
M_{12}	815 mH	C_{SE}	10 F	Compartor	
C_M	12.43 μF	L_1	1000 μH	LM393	

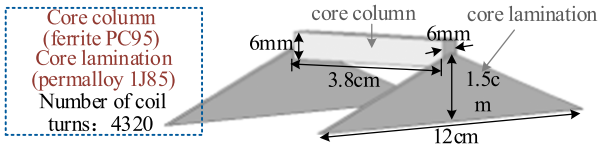

Fig. 14. FSMFEH with the triangular-shaped core lamination.

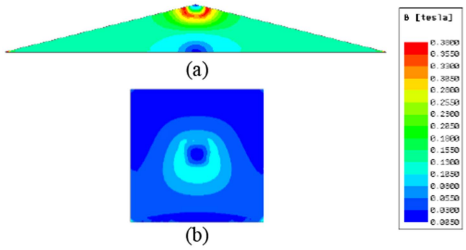

Fig. 15. Comparison of magnetic flux density distribution. (a) Triangular-shaped lamination. (b) square-shaped lamination.

central core column and core lamination on both sides. The core column, which is rectangular cuboid in shape and made of ferrite (PC95). The core lamination on both sides features a triangular cross-section. This triangular design allows the laminated core to collect more magnetic flux into the core column compared to traditional circular or square cross sections, while maintaining the same cross-sectional area. The simulation results are shown in Fig. 15, under the condition of 100 A busbar current. Besides, the core lamination is made of permalloy (1J85). The control architecture, as shown in Fig. 10, employing the STM32L476RG ultra-low-power MCU (supply current 270 μA), combined with the LM393 voltage comparator (quiescent current 200 μA) and the IVCR2405DR PWM driver chip (quiescent current 180 μA), is utilized. Besides, since V_L, $V_{\rm SE}$, and I_O are sampled, the closed-loop control can be employed by the MCU. Thus, the switches of the dc–dc converter are controlled by the MCU and PWM driver chip according to the PI calculation results of the output voltage V_L. Switches of the three-arm-rectifier are controlled by the MCU and comparators according to calculation results of the equivalent load $\rm R_{Leq}$.

B. Experimental Results

To verify the proposed theoretical model of the maximum output power point, the maximum output power waveforms under different operation modes are measured with a 100 A busbar current without the closed-loop control method. According to Fig. 16(a)–(c), the output voltages are 4.9V(@700Ω), 9.5V(@2700Ω), and 2.8V(@250Ω) under mode 1, mode 2, mode 3, respectively. Correspondingly, the maximum output powers are 34.3, 33.4, and 31.3 mW.

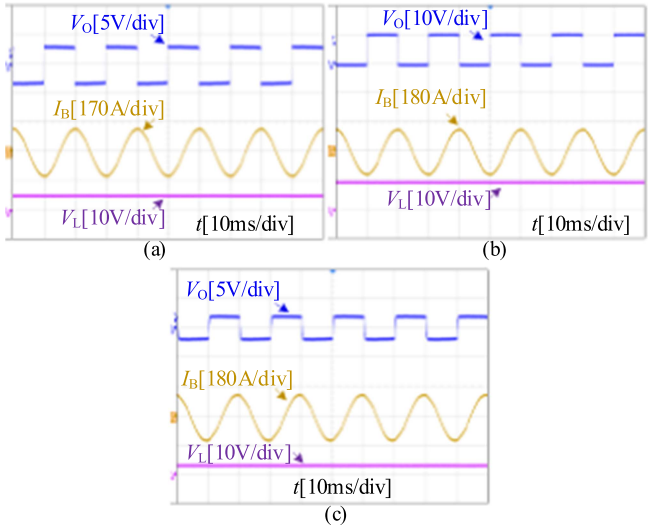

Fig. 16. Maximum output power waveforms with different modes. (a) Mode 1. (b) Mode 2. (c) Mode 3.

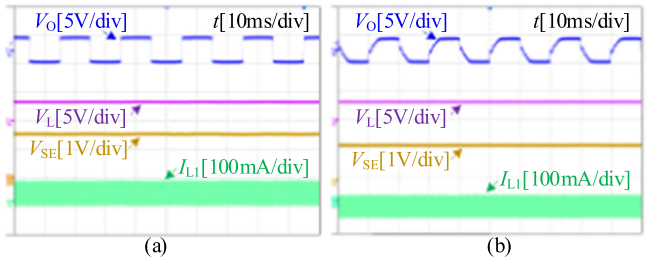

Fig. 17. Experimental waveforms of bidirectional DC–DC with different busbar currents. (a) $I_B = 100$ A. (b) $I_B = 60$ A.

In addition, the closed-loop control method of the bidirectional dc–dc is verified. As shown in Fig. 17(a), $V_{\rm SE}$ and I_{L1} denote the charging voltage and current of the SC. Take mode 1 as an example, when the busbar current is high ($I_B = 100$ A), the bidirectional dc–dc is operated in buck mode to charge the SC, and the output voltage of the load is maintained at 3.3 V. On the contrary, when the busbar current is low ($I_B = 60$ A), the bidirectional dc–dc is operated in boost mode to discharge the SC. The output voltage can still be maintained at 3.3 V, as shown in Fig. 17(b).

Output waveforms (V_L) with different cases are measured. As shown in Fig. 18, output waveforms with different busbar currents are provided. As shown in Fig. 18(a), the busbar current is 61 A, which is just high enough to power both the load and the SC, i.e., the system operates under *case* 3. As shown in Fig. 18(b), I_B changes to 100 A, the system operates under *case* 1, and output voltage can be maintained at ∼3.3 V. Under this operation condition, the equivalent load R_{Leq} is 418 Ω; thus, the FSMFEH system is operated in mode 1. When the busbar current increases to 160 A, as shown in Fig. 19(a), the equivalent load R_{Leq} is 216 Ω at this time, the operation mode

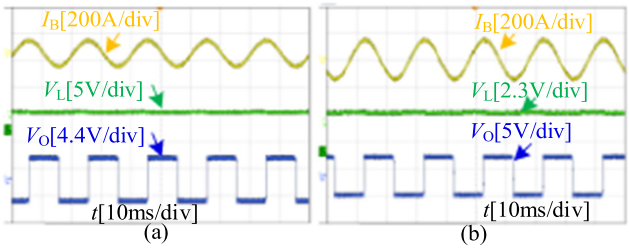

Fig. 18. Experimental waveform with different power line currents. (a) *Case* 3 $I_B = 61$ A. (b) *Case* 1 $I_B = 100$ A.

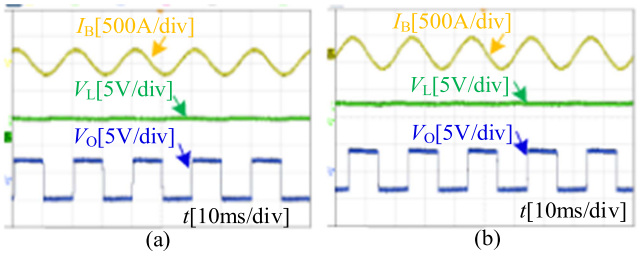

Fig. 19. Experimental waveform with different power line currents. (a) *Case* 1 $I_B = 160$ A. (b) *Case* 1 $I_B = 200$ A.

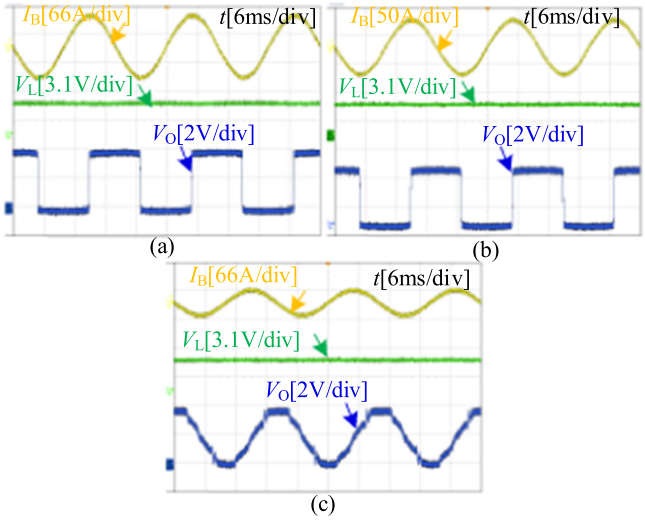

Fig. 20. The experimental waveform with different power line currents. (a) *Case* 2 $I_B = 50$ A. (b) *Case* 2 $I_B = 33$ A. (c) *Case* 2 $I_B = 20$ A.

of the FSMFEH system switches to mode 3. Furthermore, when the busbar current increases to 200 A, as shown in Fig. 19(b), the output voltage can still be maintained at ~3.3 V due to the charging of the SC. As a result, the constant voltage output is achieved under *case* 1.

Conversely, when the busbar current drops to 50 and 33 A, i.e., the system operates under *case* 2 at this time. As shown in Fig. 20(a) and (b), when the busbar current is low, the equivalent load increases accordingly, and the operation mode of the FSMFEH system will switch to mode 2. The output voltage can be maintained at ~3.3 V due to the discharging of the SC. As the busbar current is reduced, e.g., $I_B = 20$ A, as shown in

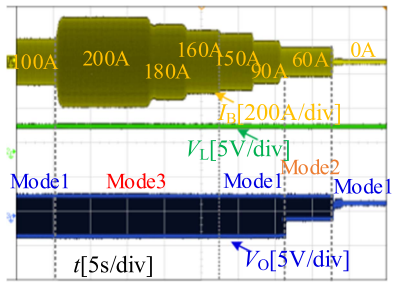

Fig. 21. Dynamic waveform with wide-range power line current variation.

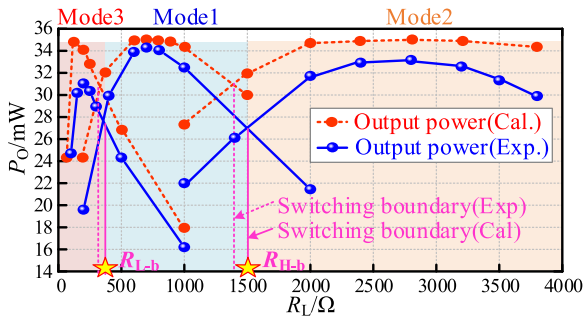

Fig. 22. Calculated and experimental output power curves ($I_B = 100$ A).

Fig. 20(c), the ac output voltage waveform is distorted. However, a 3.3 V dc output voltage can still be maintained. As a result, the constant voltage output is achieved under *case* 2.

According to Fig. 21, it can be observed that the proposed method can maintain the output voltage at ~3.3 V under varied busbar current conditions. Besides, with the increased busbar current, the equivalent load of the FSMFEH system changes accordingly. Thus, the operation mode of the system is switched from mode 2 to mode 1 and then to mode 3, which is consistent with the mode in Fig. 7. As a result, the effectiveness of the proposed strategies is validated. The calculated and experimental output power curves are plotted in Fig. 22 to verify the proposed theoretical model. It can be found that the maximum output power is 34 mW with 100 A busbar current. According to (8), (13), and (17), the maximum output power in the three modes should be the same. However, in the experiment, there exists an error of ~10% in mode 2 and mode 3 compared with the calculated results. There are two main reasons for this phenomenon. On the one hand, the mutual inductance of nonclosed magnetic cores is sensitive to the environment, resulting in different mutual inductance values under different test conditions. On the other hand, mode 2 and mode 3 have additional driving loss of switches, which led to the inconsistencies between the calculated and experimental results. It should be noted that the variation trend is the same, and the error in switching boundaries is ~7%, which proves the effectiveness of the proposed method.

The output power results with closed-loop control are plotted in Fig. 23. It shows that the proposed energy management strategies help the system to choose the optimal operation mode to improve the output power with wide-range power line current variations. When the power line current varies from 30 to 500 A,

TABLE IV
COMPARISON OF [15], [16], [18] AND THIS ARTICLE

Ref	Core volume (cm^3)	maximum output power(power density)	Working current range	Constant output voltage
Yuan et al. [15]	15×10×10	0.36 mW(0.00024 mW/cm^3)	/	No
Yuan et al. [16]	15×10×10	0.612 mW(0.000408 mW/cm^3)	/	No
Li et al. [18]	4×3×3	12 mW(0.333 mW/cm^3), I_B=100 A	100 A	No
This article	12×4×1.5	34 mW(0.472 mW/cm^3), I_B=100 A	0–500 A	Yes

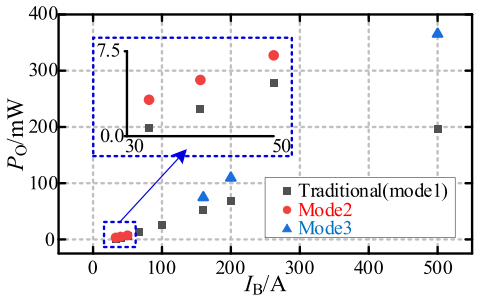

Fig. 23. Closed-loop experimental results with different power line currents.

the output power of the FSMFEH system improved from 0.6 to 3.2 mW (at min. power line current) and 109 mW with mode 3 compared with 69 mW in traditional single coil mode. When I_B = 500 A, the output power is significantly increased to 365 mW compared with the traditional mode 195 mW.

C. Comparison and Discussion

This article shares the same core objective as [15], [16], and [18], which is to improve the output power of the FSMFEH system. Their comparison is presented in Table IV. Compared to [15], [16], and [18], the advantages of this article mainly lie in two aspects: First, it achieves the constant voltage output of the FSMFEH system under wide current range conditions. Second, through the proposed method, this article achieves power improvement under wide current range variations with a smaller magnetic core size, lower cost, and simpler core manufacturing, thereby accomplishing the dual objectives of constant voltage output and power improvement. [15] and [16] only demonstrate the effect of power improvement under fixed load conditions, and the performance under wide-range loads remains unclear. However, they evidently exhibit lower output power compared to this article. In [18], within the load range of 50–1500 Ω, the maximum output power is 12 mW, and the minimum output power is 8.19 mW, resulting in a power decline percentage of 31.75%. However, this method does not account for power line current fluctuations, as the improvement results are based on fixed power line current conditions, leaving room for further refinement. In this article, through the proposed energy management method, a 3.3 V constant voltage output can be achieved when the power line current varies from 30 to 500 A. At the minimum power line current, the output power can be improved from 0.6 to 3.2 mW, and at the maximum power line current, it can be improved from 195 to 365 mW. In summary, the method proposed in this article can more effectively maintain high output power over a wide range of power line currents while simultaneously achieving constant voltage output.

V. CONCLUSION

In this article, a dual-coil and three-bridge rectifier FSMFEH system with bidirectional dc–dc is proposed. By modeling and analyzing, the output characteristics of the proposed system and switching boundaries in three modes are clarified. Based on the bidirectional dc–dc, the constant voltage output control of the dual-coil FSMFEH system can be achieved. To realize the impedance matching and improve the output power under a wide range variation of the power line current, additional switches are considered in the proposed energy management strategies to switch the operation mode of the dual-coil system and regulate the output equivalent load. The experimental results indicate that the 3.3 V constant voltage control can be achieved with different power line current conditions, and the output power can be improved from 0.6 to 3.2 mW (at min. power line current) and from 195 to 365 mW (at max. power line current).

REFERENCES

[1] V. C. Gungor, B. Lu, and G. P. Hancke, "Opportunities and challenges of wireless sensor networks in smart grid," *IEEE Trans. Ind. Electron.*, vol. 57, no. 10, pp. 3557–3564, Oct. 2010.
[2] R. Moghe, A. R. Iyer, F. C. Lambert, and D. M. Divan, "A low-cost wireless voltage sensor for monitoring MV/HV utility assets," *IEEE Trans. Smart Grid*, vol. 5, no. 4, pp. 2002–2009, Jul. 2014.
[3] Y. Li, N. Duan, Z. Liu, J. Hu, and Z. He, "Impedance-matching-based maximum power tracking for magnetic field energy harvesters using active rectifiers," *IEEE Trans. Ind. Electron.*, vol. 70, no. 10, pp. 10730–10739, Oct. 2023.
[4] D. K. Sah, A. Hazra, R. Kumar, and T. Amgoth, "Harvested energy prediction technique for solar-powered wireless sensor networks," *IEEE Sensors J*, vol. 23, no. 8, pp. 8932–8940, Apr. 2023.
[5] O. Lopez-Lapena, "Time-division multiplexing control of multi-input converters for low-power solar energy harvesters," *IEEE Trans. Ind. Electron.*, vol. 65, no. 12, pp. 9668–9676, Dec. 2018.
[6] Z. Zhang, M. Zhou, Z. Wu, S. Liu, Z. Guo, and G. Li, "A frequency security constrained scheduling approach consideringwind farm providing frequency support and reserve," *IEEE Trans. Sustain. Energy*, vol. 13, no. 2, pp. 1086–1100, Apr. 2022.
[7] I. N. Moghaddam, B. H. Chowdhury, and S. Mohajeryami, "Predictive operation and optimal sizing of battery energy storage with high wind energy penetration," *IEEE Trans. Ind. Electron.*, vol. 65, no. 8, pp. 6686–6695, Aug. 2018.
[8] Y. Li, C. Zhou, X. Wang, J. Wang, D. Qiao, and K. Tao, "A vibration energy harvester with targeted frequency-tuning capability," *IEEE Trans. Instrum. Meas.*, vol. 71, May 2022, Art. no. 7503010.

[9] Y. Li, Y. Wang, Q. Cao, J. Cao, and D. Qiao, "A self-powered vibration sensor with wide bandwidth," *IEEE Trans. Ind. Electron.*, vol. 67, no. 1, pp. 560–568, Jan. 2020.
[10] L. Liu, X. Wen, R. Shi, P. Li, Y. Wen, and T. Han, "High-efficiency magnetic field energy harvesting from a three-core cable," *Sensors Actuators A, Phys.*, vol. 360, 2023, Art. no. 114501.
[11] A. Abasian, A. Tabesh, A. Z. Nezhad, and N. Rezaei-Hosseinabadi, "Design optimization of an energy harvesting platform for self-powered wireless devices in monitoring of AC power lines," *IEEE Trans. Power Electron.*, vol. 33, no. 12, pp. 10308–10316, Dec. 2018.
[12] J. Zuo, L. Dong, F. Yang, Z. Guo, T. Wang, and L. Zuo, "Energy harvesting solutions for railway transportation: A comprehensive review," *Renew. Energy*, vol. 202, pp. 56–87, Jan. 2023.
[13] Z. Liu et al., "Mathematical modeling and optimization for the power density of the free-standing magnetic field energy harvester," *IEEE Trans. Power Electron.*, vol. 39, no. 5, pp. 6421–6432, May 2024.
[14] R. Moghe, Y. Yang, F. Lambert, and D. Divan, "Design of a low cost self powered 'stick-on' current and temperature wireless sensor for utility assets," in *Proc. IEEE Energy Convers. Congr. Expo.*, 2010, pp. 4453–4460.
[15] S. Yuan, Y. Huang, J. Zhou, Q. Xu, C. Song, and G. Yuan, "A high-efficiency helical core for magnetic field energy harvesting," *IEEE Trans. Power Electron.*, vol. 32, no. 7, pp. 5365–5376, Jul. 2017.
[16] S. Yuan, Y. Huang, J. Zhou, Q. Xu, C. Song, and P. Thompson, "Magnetic field energy harvesting under overhead power lines," *IEEE Trans. Power Electron.*, vol. 30, no. 11, pp. 6191–6202, Nov. 2015.
[17] R. Dayal, K. Modepalli, and L. Parsa, "A new optimum power control scheme for low-power energy harvesting systems," *IEEE Trans. Ind. Appl.*, vol. 49, no. 6, pp. 2651–2661, Nov./Dec. 2013.
[18] Y. Li, Y. Yan, H. Yang, J. Hu, and Z. He, "A reconfigurable rectifier-based power improving method of free-standing two-coil magnetic field energy harvesters over a wide load range," *IEEE Trans. Power Electron.*, vol. 38, no. 5, pp. 5638–5643, May 2023.
[19] K. H. K. Tse and H. S. H. Chung, "MPPT for electromagnetic energy harvesters having nonnegligible output reactance operating under slow-varying conditions," *IEEE Trans. Power Electron.*, vol. 35, no. 7, pp. 7110–7122, Jul. 2020.
[20] L. Wang, H. Wang, M. Fu, Z. Xie, and J. Liang, "Three-port power electronic interface with decoupled voltage regulation and MPPT in electromagnetic energy harvesting systems," *IEEE Trans. Ind. Appl.*, vol. 58, no. 2, pp. 2144–2154, Mar./Apr. 2022.
[21] Y. Chen, S. He, B. Yang, S. Chen, Z. He, and R. Mai, "Reconfigurable rectifier-based detuned series-series compensated IPT system for anti-misalignment and efficiency improvement," *IEEE Trans. Power Electron.*, vol. 38, no. 2, pp. 2720–2729, Feb. 2023.
[22] Z. Liu, Y. Li, N. Duan, and Z. He, "An energy management method for magnetic field energy harvesters under wide-range current in railway electrification systems," *IEEE Trans. Ind. Electron.*, vol. 71, no. 5, pp. 5360–5369, May 2024.

Huanyu Yang received the B.Sc. and Ph.D. degrees in electrical engineering and automation from the School of Electrical Engineering, Southwest Jiaotong University, Chengdu, China, in 2018 and 2024, respectively.

He is currently an Engineer with Hunan Disaster Prevention Technology Company, Ltd. Changsha, China. His main research interests include wireless power transfer and energy harvesting

Yuhang Liu received the B.S. degree in electrical engineering and automation from the School of Southwest University of Science and Technology, Mianyang, China, in 2021. He is currently working toward the Ph. D. degree in electrical engineering with Southwest Jiaotong University, Chengdu, China.

His main research interests include wireless power transfer and energy harvesting

Yong Li (Senior Member, IEEE) received the B.Sc. and Ph.D. degrees in electrical engineering from the School of Electrical Engineering, Southwest Jiaotong University, Chengdu, China, in 2013 and 2017, respectively.

From 2017 to 2018, he was a Research Associate with the Department of Electrical Engineering, The Hong Kong Polytechnic University, and subsequently, he was a Post-Doctoral Fellow. He is currently a Professor with the School of Electrical Engineering, Southwest Jiaotong University. His main research interests include wireless power transfer and energy harvesting.

Yonghong Zhou received the B.Sc. degree in electrical engineering and automation from the School of Electrical Engineering, Qingdao University, Qingdao, China, in 2023. He is currently working toward the M.Sc. degree in electrical engineering with the School of Electrical Engineering, Southwest Jiaotong University, Chengdu, China.

His primary research focus is magnetic field energy harvesting, particularly enhancing the power density of free-standing magnetic field energy harvesters.

Zhengyou He (Senior Member, IEEE) received the B.Sc. and M.Sc. degrees in computational mechanics from Chongqing University, Chongqing, China, in 1992 and 1995, respectively, and the Ph.D. degree in electrical engineering from the School of Electrical Engineering, Southwest Jiaotong University, Chengdu, China, in 2001.

He is currently a Professor with the School of Electrical Engineering, Southwest Jiaotong University. His research interests include signal process and information theory applied to electrical power system, and application of wavelet transforms in power systems.